Nano Research

ISSN 1998-0124 CN 11-5974/O4
https://doi.org/10.1007/s12274-019-2602-6

Research Article

NaV_6O_{15}: a promising cathode material for insertion/extraction of Mg^{2+} with excellent cycling performance

Dongzheng Wu[1], Jing Zeng[1], Haiming Hua[1], Junnan Wu[1], Yang Yang[2] (✉), and Jinbao Zhao[1] (✉)

[1] *Collaborative Innovation Center of Chemistry for Energy Materials, State Key Lab of Physical Chemistry of Solid Surfaces, State-Province Joint Engineering Laboratory of Power Source Technology for New Energy Vehicle, Engineering Research Center of Electrochemical Technology, Ministry of Education, College of Chemistry and Chemical Engineering, Xiamen University, Xiamen 361005, China*
[2] *School of Chemical Engineering and Light Industry, Guangdong University of Technology, Guangzhou 510006, China*

Received: 17 September / **Revised:** 12 November 2019 / **Accepted:** 10 December 2019

ABSTRACT

The rechargeable magnesium batteries (RMBs) are getting more and more attention because of their high-energy density, high-security and low-cost. Nevertheless, the high charge density of Mg^{2+} makes the diffusion of Mg^{2+} in the conventional cathodes very slow, resulting in a lack of appropriate electrode materials for RMBs. In this work, we enlarge the layer spacing of V_2O_5 by introducing Na^+ in the crystal structure to promote the diffusion kinetics of Mg^{2+}. The NaV_6O_{15} (NVO) synthesized by a facile method is studied as a cathode material for RMBs with the anhydrous pure Mg^{2+} electrolyte. As a result, the NVO not only exhibits high discharge capacity (119.2 $mAh\cdot g^{-1}$ after 100 cycles at the current density of 20 $mA\cdot g^{-1}$) and working voltage (above 1.6 V vs. Mg^{2+}/Mg), but also expresses good rate capability. Besides, the *ex-situ* characterizations results reveal that the Mg^{2+} storage mechanism in NVO is based on the intercalation and de-intercalation. The density functional theory (DFT) calculation results further indicate that Mg^{2+} tends to occupy the semi-occupied sites of Na^+ in the NVO. Moreover, the galvanostatic intermittent titration technique (GITT) demonstrates that NVO electrode has the fast diffusion kinetics of Mg^{2+} during discharge process ranging from 7.55×10^{-13} to 2.41×10^{-11} $cm^2\cdot s^{-1}$. Our work proves that the NVO is a potential cathode material for RMBs.

KEYWORDS

NaV_6O_{15}, alkali metal pre-intercalation, rechargeable magnesium battery, cathode, electrochemical mechanism

1 Introduction

The high performance and long-life energy storage systems play an important role in energy strategy [1, 2]. In the past two decades, the lithium ion batteries (LIBs) have been widely studied as an excellent energy storage system, but the concerns of safety problem and high price have always been the bottleneck of the system [3–7]. As an alternative to the LIBs, the rechargeable magnesium batteries (RMBs) have a great potential for the large-scale energy storage applications because of its high-security, low price, and high volumetric energy density [8–12]. However, the development of RMBs is still in its infancy. The cathode is an important part of the battery. However, most of the cathode materials suitable for the LIBs or sodium ion batteries (SIBs) show poor capacity and cycle stability in RMBs because the high charge density of Mg^{2+} causes a slow diffusion rate of Mg^{2+} in the electrode [13–16]. Therefore, in order to improve the energy density of RMBs to meet the demands of application, finding a suitable cathode material with good electrochemical performance has become a challenge which must be overcome [17–20].

Researchers have made a lot of efforts to find an applicable cathode material to improve the electrochemical performance and cycle life of RMBs [21–23]. For instance, the Chevrel phase compound Mo_6S_8 reported by Aurbach exhibits an excellent reversibility in RMBs (80 $mA\cdot g^{-1}$ after 2,000 cycles, working voltage ~ 1.1 V), but its low working voltage and capacity can only provide limited energy density [21]. Besides, many materials such as CuS and MnO_2 have been reported in RMBs recently, but their electrochemical performance, stability and energy density are still far from satisfying the needs for the commercialization of RMBs [22, 23].

In order to enhance the energy density of RMBs, increasing the operating voltage and specific capacity is an effective method. To our knowledge, the metal oxides are a class of materials with high specific capacity and high working voltage. Among them, V_2O_5 is considered a promising cathode material in the LIBs and SIBs [24–27]. Therefore, scientists have also conducted a lot of exploration on the application of V_2O_5 in RMBs [27–35]. In 1993, Novak et al. applied V_2O_5 to RMBs in magnesium perchlorate electrolyte with a capacity of 170 $mAh\cdot g^{-1}$. However, its capacity decayed rapidly which may be due to the interaction between Mg^{2+} and V_2O_5 matrix material [27]. In order to accelerate the diffusion of Mg^{2+} and improve the storage capacity of Mg^{2+} in V_2O_5, several strategies were proposed: (i) water was introduced to the electrolyte, or introduced to the crystal structure of the V_2O_5 [30, 31]. (ii) Increasing the interlayer spacing of V_2O_5 by the pre-intercalation of polymer or alkali metal ion was also effective [32–35]. However, these methods still have some problems in practice. Water will react with Mg anode and create

---

Address correspondence to Yang Yang, yangyang@gdut.edu.cn; Jinbao Zhao, jbzhao@xmu.edu.cn

a passive film on the Mg anode, impeding the dissolution/deposition of magnesium on anode side, which in turn leads to a deactivation of the battery [31]. Even if water is introduced into the crystal structure, the crystal water is also likely to be released during the long-term cycle, and will react with the Mg anode [28]. In 2017, Perera et al. incorporated poly(ethylene oxide) (PEO) to expand the interlayer spacing of $V_2O_5{\cdot}nH_2O$ for improving the storage performance of magnesium, but the cycling performance is limited [32]. Recently, Rashad et al. proposed the preparation of $NaV_3O_8{\cdot}1.69H_2O$ with Na^+ intercalation, and served it as the cathode in RMBs, and the $NaV_3O_8{\cdot}1.69H_2O$ showed a good performance in the magnesium full cells (110 $mAh{\cdot}g^{-1}$, 10 $mA{\cdot}g^{-1}$, 80% capacity retention after 100 cycles) but the crystal water was still introduced [33]. Subsequently, Tang et al. studied the preparation of the V_3O_8 materials with different alkali metal ion pre-intercalation [34]. Their theoretical calculation and experimental results showed that the pre-inserted Na-V_3O_8 had excellent specific capacity and cycle stability (after 30 cycles, the capacity was 175 $mAh{\cdot}g^{-1}$, and the capacity retention rate was 85.78%). The reason why the Na-V_3O_8 has better Mg^{2+} storage performance than the Li^+ or K^+ pre-intercalation is that the pre-insertion of Na^+ reduces the diffusion energy barrier of Mg^{2+} in the host material, and stabilizes the structure of V_3O_8 during the discharge and charge process, indicating the pre-intercalation of alkali metal ion is an effective method for improving the storage properties of magnesium.

Herein, we have prepared the Na^+ pre-intercalated NVO with larger layer spacing and free of crystal water by a simple and rapid method, and applied the NVO to the magnesium battery with anhydrous electrolyte. Actually, Cabello et al. first proved the successful insertion of Mg^{2+} in NVO [36]. However, the electrochemical performance was poor (working voltage ~0.8 V vs. Mg^{2+}/Mg), which might be caused by the test system. The electrolyte $Mg(ClO_4)_2$ in acetonitrile (AN) is incompatible with Mg metal anode. Even if the electrolyte $NaBH_4$-$Mg(BH_4)_2$ in diglyme was introduced, the NVO showed a declining capacity of around 80 $mAh{\cdot}g^{-1}$ after 30 cycles at 15 µA. Moreover, the behavior of Mg inside NVO is not very much clear. Hence, a suitable system is needed to reassess the magnesium storage properties of the NVO, and further study the storage mechanism of Mg^{2+} in the pure Mg^{2+} electrolyte. According to the literature, the active carbon (AC) electrode could be a quasi-reference electrode with the potential of 2.45 V vs. Mg^{2+}/Mg [37].

In this work, as expected, the NVO material maintains a high discharge capacity of 119.2 $mAh{\cdot}g^{-1}$ after 100 cycles at 20 $mA{\cdot}g^{-1}$. In addition, the insertion and extraction mechanism and diffusion kinetics of Mg^{2+} in NVO have been researched more comprehensively. Furthermore, combined with theoretical calculations, the internal inlaid magnesium position of NVO is studied.

2 Experiment

2.1 Synthesis of NVO

The NVO were prepared by a facile and low-cost method, which was reported by Jiang et al. before [38]. For a typical synthesis experiment, 0.702 g NH_4VO_3 and 0.085 g $NaNO_3$ were added to 10 mL water. The mixture solution was continually stirred and heated at 80 °C to acquire a clear yellow solution. After the addition of 2.2 g citric acid, the solution immediately turned dark green and finally turned blue. The mixed solution was constantly stirred until the solvent was evaporated. The product was calcined in an air atmosphere at 450 °C for 4 h. The heating rate is 5 $°C{\cdot}min^{-1}$. Finally, the dark brown NVO powder was obtained.

2.2 Physical characterizations

The crystallographic information was measured by using X-ray diffraction (XRD, Rigaku Corporation, Japan) with a Cu $K\alpha$ radiation. The scanning electron microscopy (SEM) images were conducted on the Hitachi S-4800. Transmission electron microscope (TEM) images were acquired by the JEM-2100 and FEI TECNAI G2 F30. The X-ray photoelectron spectroscopy (XPS) was obtained from the PHI Quantum 2000.

2.3 Electrochemical tests

A slurry composed of 70 wt.% NVO, 20 wt.% acetylene black and 10 wt.% polyvinylidene fluoride (PVDF) in N-methyl-2-pyrrolidinone (NMP) was casted on a Ti foil, followed by drying at 80 °C about 12 h to remove the solvent. The mass loading of working electrodes was between 1.0 and 1.5 $mg{\cdot}cm^{-2}$ for the electrochemical tests. The active carbon, acetylene black and PVDF at a weight ratio of 8:1:1 in NMP were used to prepare the active carbon electrodes. The electrochemical tests were evaluated with the CR2032 coin cells, using the Celgard 2400 separator and the 0.5 M $Mg(ClO_4)_2$/acetonitrile electrolyte. The NVO electrode was the cathode, and the AC electrode was the reference electrode and counter electrode. The anhydrous electrolyte was prepared for the electrochemical performance test. For the preparation of the anhydrous electrolyte, firstly, $Mg(ClO_4)_2{\cdot}6H_2O$ was dried at 200 °C for 1 h to remove the crystal water, and then dissolved in anhydrous AN. Then molecular sieves were added to the electrolyte to further remove water for several times. The cyclic voltammetry (CV) tests were conducted on an electrochemical workstation (CHI 1030C, Chenhua). The galvanostatic charge-discharge tests and galvanostatic intermittent titration technique (GITT) tests were measured in the potential range of −0.8–0.5 V vs. AC. Before the electrochemical test, the NVO electrode was activated for 5 cycles at 10 $mA{\cdot}g^{-1}$. In the GITT test, typically, battery was discharged and charged at 10 $mA{\cdot}g^{-1}$ for 600 s (τ) and stood for one hour, repeating until discharged to −0.8 V vs. AC or charged to 0.5 V vs. AC. All the electrochemical measurements of the half cell and the full cell were tested at 25 °C.

2.4 Theoretical calculations

All the density functional theory (DFT) calculations were performed with the Vienna *Ab initio* Simulation Package (VASP) [39]. We used the GGA functional PBE with the PAW pseudopotentials [40, 41]. The Hubbard U-corrections in the rotationally invariant form was used to correct the self-interaction energy, and the U-J value for V element was set to 3.1 eV [42]. The energy cutoff for plane wave basis was set to 500 eV. The spin polarization with ferromagnetic (FM) spin ordering first guess was set for all calculations. The optimization thresholds were set as 10^{-5} eV for electronic relaxations and 0.02 $eV{\cdot}Å^{-1}$ for ionic relaxations. The Gaussian smearing with a smearing factor of 0.1 eV was used. All atoms positions and unit cells were fully relaxed in the geometric optimizations. We gained the crystal structure of NVO from the Crystallography Open Database (COD) and Materials Project. The initial unit cell parameter is: a = 15.73 Å, b = 7.33 Å, c = 10.27 Å, $\alpha = \gamma$ = 90.00°, β = 109.68°, and there are 88 atoms in the cell. The 2 × 5 × 3 Monkhorst-Pack k-points mesh was used [43]. The voltage and the site of Mg^{2+} insertion are calculated by inserting Mg atoms into the semi-occupied sites of Na atoms, 4-coordination holes and 8-coordination holes in the primary crystal. All the structures were visualized by the VESTA software [44]. The voltage of Mg^{2+} insertion for $NaMg_xV_6O_{15}$ was calculated as:

$$V = -\frac{E_{X_2} - E_{X_1} - (X_2 - X_1)E_{Mg}}{2(X_2 - X_1)F} \quad (1)$$

3 Result and discussions

3.1 Physical characterizations of the NVO

The XRD pattern of the as-prepared NVO is exhibited in Fig. 1(a). All the diffraction peaks match well with a monoclinic NVO phase [space group: *A*2/*m*, JCPDS. No. 077-0146], indicating the successful synthesis of NVO powder without any impurities. The Fig. 1(a) inset demonstrates the crystal structure of the layered monoclinic phase NVO, where Na^+ between layers as a support, which improves the stability of the NVO layered structure. Moreover, there are still many vacancies between the layers of NVO for the ion insertion [45]. The morphology and microstructure of the NVO are revealed in Figs. 1(b) and 1(c). The NVO sample is consist of rod-like particles with the length of 250 nm–4 μm and a diameter of 100–250 nm. And the elemental mapping result (Fig. S1 in the Electronic Supplementary Material (ESM)) demonstrates that Na, V, and O are uniformly distributed within the NVO. The high resolution TEM (HRTEM) image (Fig. 1(d)) exhibits the clear lattice fringes of 0.73 and 0.22 nm, corresponding to the (002) and (106) planes of monoclinic NVO respectively, and confirming the good crystallinity of NVO. Moreover, the XPS spectrum Na 1s and V 2p of the NVO powder is shown in Figs. 1(e) and 1(f). It can be seen that Na^+ is successfully introduced to the NVO, and the peaks located at 517.3, 524.5, 515.6, and 523.5 eV are indexed to V^{5+} $2p_{3/2}$, V^{5+} $2p_{1/2}$, V^{4+} $2p_{3/2}$ and V^{4+} $2p_{1/2}$, respectively. The existence of V^{4+} in initial sample is caused by the reduction of citric acid and the presence of Na^+ for neutrality [38]. The above analyses prove the successful preparation of NVO materials.

3.2 Electrochemical performances

It has been reported that the NVO has excellent electrochemical properties in the SIBs [38]. Moreover, the sodiation/desodiation mechanism of NVO is insertion-type without obvious phase transition during cycling [17, 46]. Thus, the NVO may be a promising cathode material for RMBs. The Fig. 2(a) exhibits the typical charge-discharge curves of the NVO at 10 mA·g^{-1}. There is no obvious platform for the discharge curves, and two platforms occur in the charge curves, indicating that the insertion of Mg^{2+} takes place in one step while the extraction of Mg^{2+} experiences two steps. The initial discharge capacity is 213.4 mAh·g^{-1} with a Coulombic efficiency of 82.8%, which is slightly lower than that of NVO in the LIBs and SIBs. The Coulombic efficiency gradually increases to 96.5% after 5 cycles, attributing to the activation process in the NVO for RMBs. The Fig. 2(b) presents the CV curves of the first three circles, offering a better understanding of the magnesiated/demagnesiated and activation process. It can be seen that the magnesiated process takes place in between −0.8 V–−0.4 V vs. AC, while the demagnesiated process shows one weak peak at −0.3 V vs. AC and one sharp peak at 0.2 V vs. AC, which indicates that the demagnesiated process is divided into two steps, and the extraction of Mg^{2+} happens at around 0.2 V vs. AC mainly. Besides, the peak area increases after 3 cycles, corroborating that the existence of the activation process during the first several cycles. Encouragingly, the NVO not only exhibits a high discharge specific capacity, but also presents excellent long-term cycling stability and good rate capability (Figs. 2(c) and 2(d)). Almost no capacity decay is observed after 80 cycles at 20 mA·g^{-1}. Moreover, after 100 cycles, the NVO still delivers 119.2 mAh·g^{-1} and maintains the higher capacity retention rate. The Coulombic effiency is greater than 100% during the stable cycle, which may be due to the expansion or contraction of the crystal lattice resulting in the extraction of trace amounts of Mg^{2+} from the NVO crystal structure and the decomposition of the electrolyte. As shown in Fig. 2(d), the discharge specific capacities of NVO are 210.1, 137.0, 111.7, 80.2, 52.3, and 27.2 mAh·g^{-1} at 10, 20, 50, 100, 200, and 500 mA·g^{-1}, respectively. Deserved to be mentioned, the NVO electrode delivers a high capacity of around 140 mAh·g^{-1} when the current density return to 20 mA·g^{-1}. As the specific capacity, operating voltage and capacity retention are considered comprehensively, the electrochemical performance of as-prepared NVO is prominent compared with some RMB cathode materials previously reported (Table S1 in the ESM). In addition, the electrochemical performance of NVO in 0.5 M $Mg(ClO_4)_2$/AN (Fig. S2 in the ESM) and $(PhMgCl)_2/AlCl_3$/THF (APC) electrolyte (Fig. S3 in the ESM), respectively, with

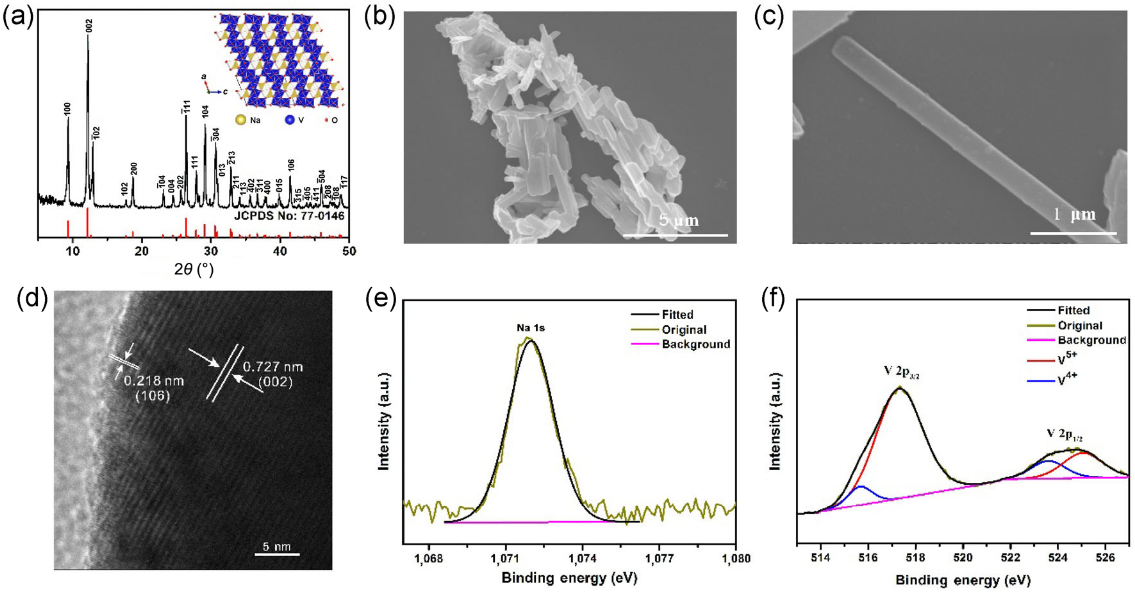

Figure 1 (a) XRD pattern of the NVO powder and crystal structure of the NVO (inset). (b) and (c) SEM images of the NVO at different magnification. (d) HRTEM image of the NVO powder. XPS spectra of (e) Na 1s and (f) V 2p of the NVO powder.

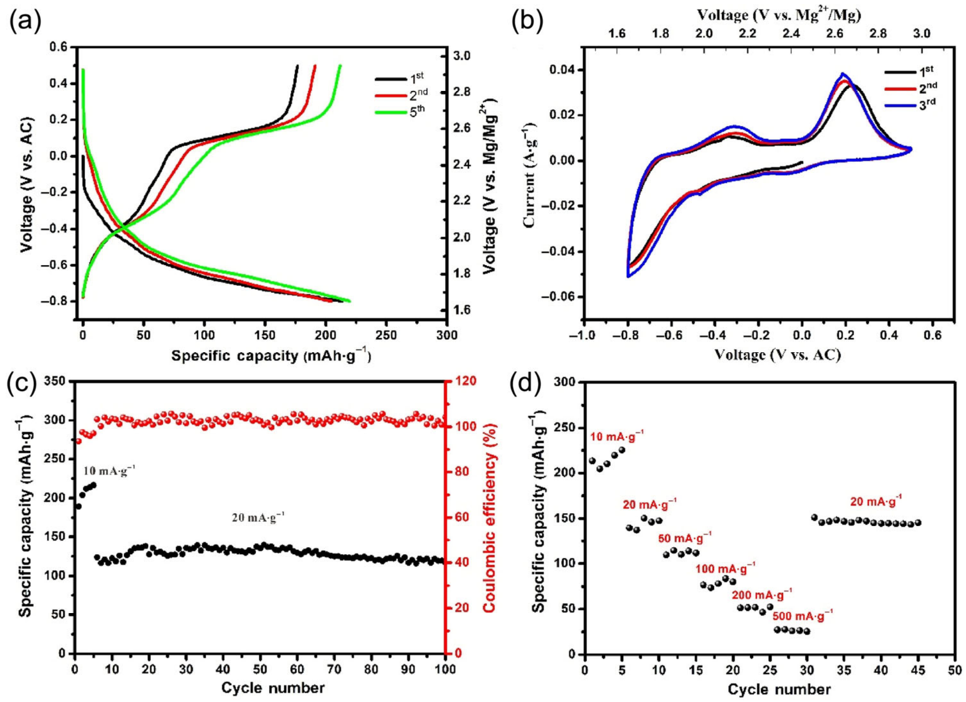

Figure 2 (a) Charge-discharge profiles of the NVO at 10 mA·g−1. (b) CV curves of the first three cycles. (c) Cycling stability of the NVO at 20 mA·g−1. (d) Rate capability of the NVO.

magnesium anode has been also measured. However, the NVO has a high specific capacity and good cycling performance within 20 cycles in 0.5 M $Mg(ClO_4)_2$/AN with Mg anode, but this electrolyte will lead to a thick passive film on the Mg anode which is dense and does not allow Mg^{2+} to pass through, leading to the bad electrochemical performance after 20 cycles [47]. As for APC electrolyte, we only get a low discharge specific capacity and the NVO cannot exhibit its inherent electrochemical performance due to the incompatibility between the APC electrolyte and the NVO electrode [48].

3.3 Electrochemical reaction mechanism

To further understand the electrochemical reaction mechanism of the NVO for the Mg^{2+} storage, the *ex-situ* XRD measurements have been operated (Figs. 3(a)–3(c). The peaks at 35.06°, 38.40° and 40.15° originate from the Ti foil substrate. As shown in Fig. 3(b), there are no new peaks appearing or disappearing during the magnesiated and demagnesiated processes from −0.8 to 0.5 V vs. AC, indicating a typical insertion-type Mg^{2+} storage mechanism, which is similar to the NVO for the LIBs and NIBs [36, 38, 49–51]. The Fig. 3(c) is an enlarged version of the NVO electrodes between 11.5° and 13.5°. Firstly, when the NVO electrode is discharged from initial state to −0.5, and −0.6 V, the main peak (002) of NVO at 12.16° shifts to a higher angle of 12.18°, and 12.24°, respectively, caused by mutual effect between Mg^{2+} and oxygen in the host material. But as the NVO electrode is further discharged to −0.8 V, the peak of (002) plane shifts from 12.24° to 12.20°, illustrating the increase of layer distance, which is on account of the large electrostatic repulsion caused by the insertion of more Mg^{2+}. In the charge process, the peak (002) shifts to a higher angle of 12.24° (charged to −0.4 V) firstly, then to 12.28° (charged to −0.2 V), showing the decrease of electrostatic repulsion due to the extraction of Mg^{2+}. When the NVO electrode is charged to 0.2 V, the peak (002) shifts to 12.20°. Moreover, as the NVO electrode is fully charged, the peak (002) finally returns to

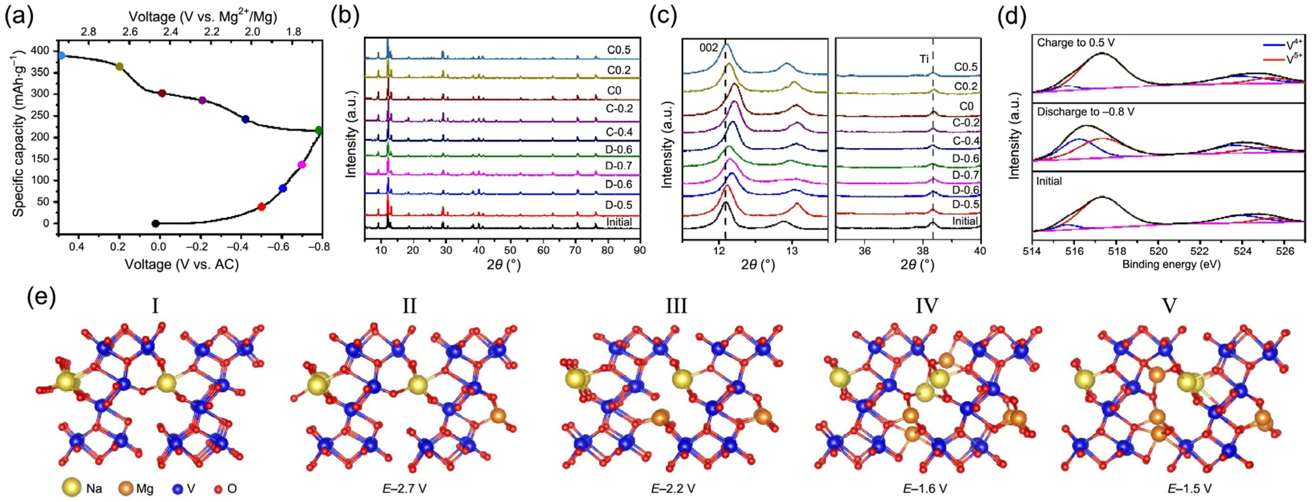

Figure 3 (a) Charge-discharge curves of the NVO. (b) *Ex-situ* XRD of NVO electrodes at different charge and discharge states. (c) Local enlarged image at different charge-discharge status. (d) XPS spectra of V at the different state of the NVO electrode. (e) The DFT calculation results.

the initial angle, indicating the excellent reversibility of NVO structure during cycling. The similar crystal structure evolution processes were also reported in the pre-inserted Na-V_3O_8 [34]. During the discharge and charge process, the volume changes of NVO are shown in Table S4 in the ESM. When the NVO electrode is discharged to −0.6 V (vs. AC) or charged to 0 V (vs. AC), there are only minor changes of layer spacing during the insertion/extraction of Mg^{2+} indicating the excellent structural stability of NVO. The XPS at different charging state was also collected to further demonstrate the valence state change of vanadium during magnesiated and demagnesiated process. During the whole electrochemical cycling of the NVO electrode, the valence of vanadium is only changed between V^{5+} and V^{4+} (Fig. 3(d)). When the NVO electrode is discharged to −0.8 V vs. AC, the ratio of V^{4+}/V^{5+} is increased remarkably, indicating the successful insertion of Mg^{2+}. When the NVO electrode is charged to 0.5 V vs. AC, all peaks return back to the initial values coherent with the initial electrode, representing the excellent reversibility of NVO electrode.

In order to further study the specific insertion site of Mg^{2+} in the NVO, the DFT calculation has been carried out. The results of the DFT study (Fig. 3(e)) indicate that Mg^{2+} preferentially occupies the semi-occupied sites of Na and the average voltage of insertion is 2.2 V during the first discharge stage. While the semi-occupied sites of Na are filled with Mg^{2+}, other Mg^{2+} tend to occupy the four-coordination channel and eight-coordination channel, and the corresponding voltage of Mg^{2+} insertion is shown in Fig. 3(e), respectively. The calculation results are consistent with the experimental results. According to the above analysis, it has given us a richer understanding of the magnesiated/demagnesiated process in the NVO.

The TEM results of NVO electrodes are presented in Figs. 4(a)–4(f) to investigate the changes of crystal structure during the magnesiated and demagnesiated process. The Fig. 4(a) exhibits the morphology of initial NVO electrode. The initial NVO electrode exhibits the lattice fringe spacing of 0.20 nm, corresponding to the $50\bar{4}$ plane of the monoclinic phase NVO (Fig. 4(d)). The morphology and crystal structure of NVO discharged to −0.8 V vs. AC are shown in Figs. 4(b) and 4(e). After discharging, the lattice fringe spacing of $50\bar{4}$ plane is slightly reduced, indicating the lattice contraction of NaV_6O_{15}. Since the influence of the insertion of Mg^{2+} on the $50\bar{4}$ plane is very small, only minor change in the lattice fringe can be observed. When the NVO electrode is charged to 0.5 V vs. AC, the TEM image and the lattice fringe of NVO are consistent with the initial electrode, indicating the good reversibility of NVO during magnesiated and demagnesiated process. Furthermore, the elemental mapping results of the fully discharged NVO electrode shows that the Na, V, O and Mg elements are uniformly distributed, indicating the Mg^{2+} ions are inserted in the NVO host material successfully.

The ion diffusion coefficient in host material plays an important role in the battery system, which is essential for electrochemical performance. In order to have a good knowledge of the diffusion behavior of Mg^{2+} in NVO, the GITT measurements have been carried out. The Mg^{2+} diffusion coefficients ($D_{Mg^{2+}}$) in NVO can be obtained from the experiment results (Fig. 5(a)) by Eq. (2)

$$D_{\mathrm{Mg}^{2+}} = \frac{4}{\pi\tau}\left(\frac{m_{\mathrm{B}}V_{\mathrm{m}}}{M_{\mathrm{B}}A}\right)^2\left(\frac{\Delta E_{\mathrm{S}}}{\Delta E_{\tau}}\right)^2\left(\tau \ll \frac{L^2}{D_{\mathrm{Mg}^{2+}}}\right) \qquad (2)$$

Where m_B and M_B are the mass loading (g) and molecular weight ($g \cdot mol^{-1}$) of the NVO, respectively, V_m is the molar volume of NVO (159.28 $cm^3 \cdot mol^{-1}$), A is the surface area of electrode, ΔE_S is the potential difference of the steady-state voltage during the rest process, ΔE_τ is the potential change through a discharge pulse without including IR drop, L is the thickness of the electrode (cm) [52]. The calculation result of $D_{Mg^{2+}}$ at different discharge and charge potential is demonstrated in Fig. 5(b). The Mg^{2+} diffusion coefficients range from 7.55×10^{-13} to 2.41×10^{-11} $cm^2 \cdot s^{-1}$ in the potential range of −0.8–0 V vs. AC during the discharge process, indicating the larger layer spacing facilitates the diffusion of Mg^{2+}. While the Mg^{2+}

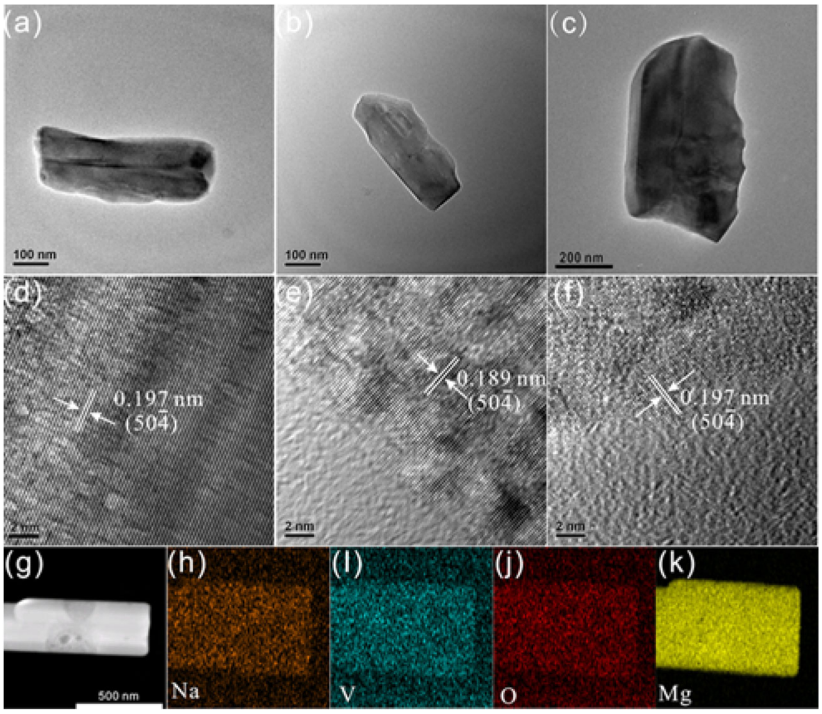

Figure 4 (a)–(c) TEM images of the initial NVO electrode, the discharged NVO electrode and the charged NVO electrode, respectively. (d) and (f) HRTEM images corresponding to (a)–(c). (g) High-angle annular dark field STEM (HAADF-STEM) image of the NVO electrode discharged to −0.8 V. (h)–(k) Corresponding to the elemental mapping of Na, V, O, and Mg, respectively.

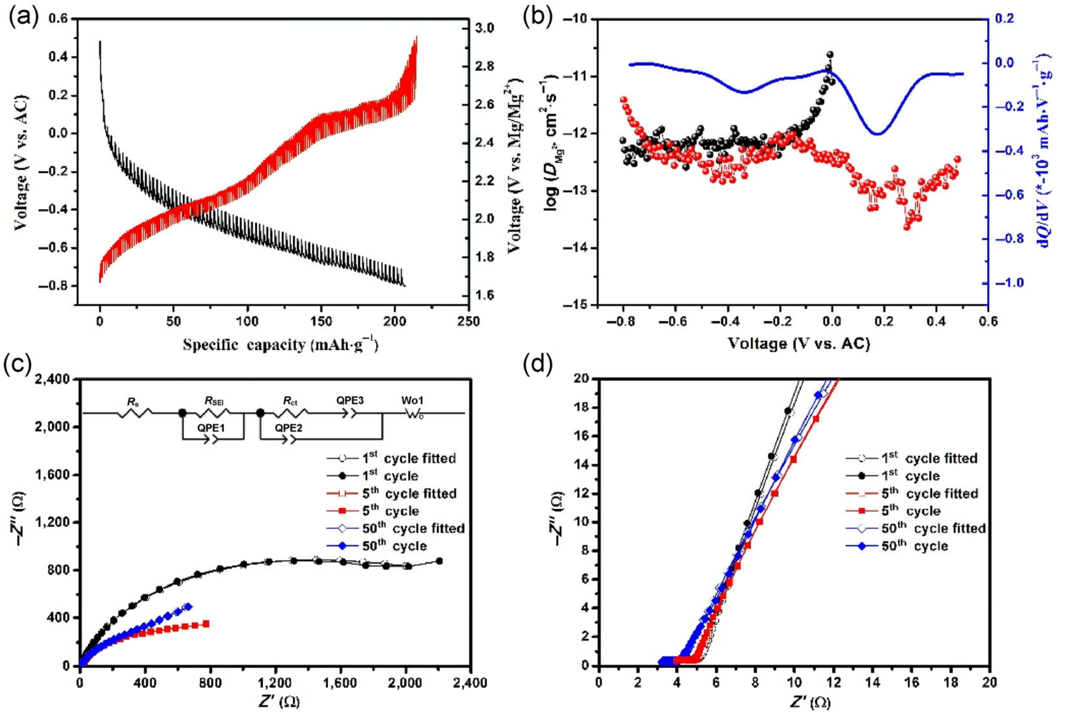

Figure 5 (a) The GITT curve of NVO at 10 mA·g^{-1} during discharge and charge processes. (b) Corresponding to the diffusion coefficients of Mg^{2+}and the dQ/dV curve calculated from the actual charge curve. (c) Nyquist plots of the different cycled NVO electrode and fitted curves; and equivalent circuit (inset). (d) Enlarged image of the high frequency region.

diffusion coefficients range from 2.32×10^{-14} to 3.88×10^{-12} cm^2·s^{-1} in the potential range of −0.8–0.5 V vs. AC during the charge process. The trend of $D_{\mathrm{Mg}^{2+}}$ is similar with the dQ/dV curve in charge process, indicating the $D_{\mathrm{Mg}^{2+}}$ is lower at the reaction platform, which is consistent with previous reports [52–55]. Obviously, the Mg^{2+} diffusion coefficients in discharge process are much larger than that in charge process, indicating the magnesiated process is much easier than demagnesiated process. To sum up, the NVO presents fast diffusion kinetics of Mg^{2+}, which benefits from Na$^+$ pre-intercalation, and it means that this is a useful way to enhance the storage property of Mg^{2+}. The fast Mg^{2+} diffusion rate in the NVO electrode is the main cause of the prominent electrochemical performance of NVO in RMBs.

To get deep insights into the superior long-term cycling stability, the electrochemical impedance spectroscopy (EIS) test has been performed. The Figs. 5(c) and 5(d) shows the Nyquist plots of the different cycled NVO electrode, respectively. They are all composed of two compressed semicircles in the high-middle frequency region. All of them can be well fitted by an equivalent circuit. The fitted data are shown in the Table S2 in the ESM. The intersection (R_{S}) of the curve and the X axis in the high frequency region represents the resistance inside the battery. The semicircle in the high frequency region corresponds to the resistance of interface R_{SEI} and capacitance QPE1, which are related to the solid electrolyte interphase (SEI). The semicircle in the middle frequency region corresponds to the resistance of charge transfer R_{ct} and capacitance QPE2 and QPE3, which are related to the transition of Mg^{2+}. The oblique line corresponds to Wo1 representing the diffusion of Mg^{2+} in solid phase. It is easy to acquire that the R_{S} and R_{SEI} are almost unchanged. However, the first cycled electrode has a large R_{ct} (2,394 Ω), and the electrode after 5 cycles has a much smaller R_{ct} (541.6 Ω). It is interesting that the NVO still delivers a small R_{ct} (205.9 Ω) after 50 cycles. The R_{ct} decrease after electrochemical behavior indicates that the existence of the activation process and the importance of Na$^+$ between layers for the stability of NVO electrode. Similar activation processes of metal oxide were also reported in the batteries [35, 56]. Moreover, the SEM images of the NVO electrode before and after cycling have been also performed to check the stability of the NVO electrode during cycling. As shown in Figs. 6(c) and 6(d), after 50 cycles, the morphology and microstructure of the NVO are a rod-like structure similar to that of pristine NVO electrode (Figs. 6(a) and 6(b)). The results of SEM images indicate the excellent structural stability of the NVO for RMBs.

3.4 Stability of sodium ion in NVO

The Na$^+$ is considered to be an important component for stabilizing the crystal structure of NVO. Therefore, confirming whether Na$^+$ is extracted during cycling in RMBs is critical. As shown in Fig. 7(a), no capacity is presented in as-prepared SIB until the decomposition voltage of the electrolyte is reached,

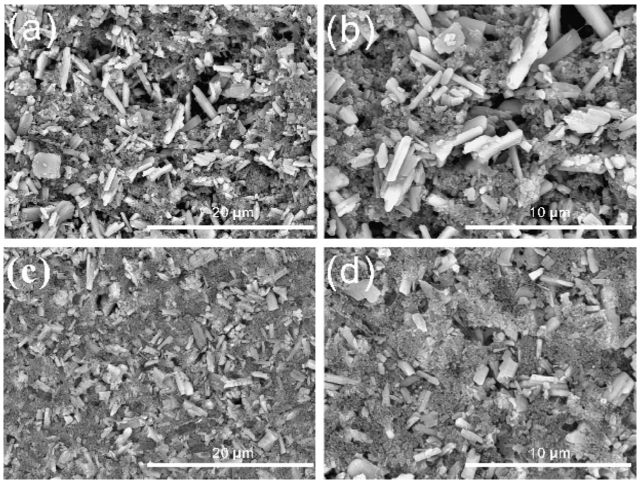

Figure 6 (a) and (b) SEM images of the NVO electrode at the initial state. (c) and (d) SEM images of the NVO electrode after 50 cycles.

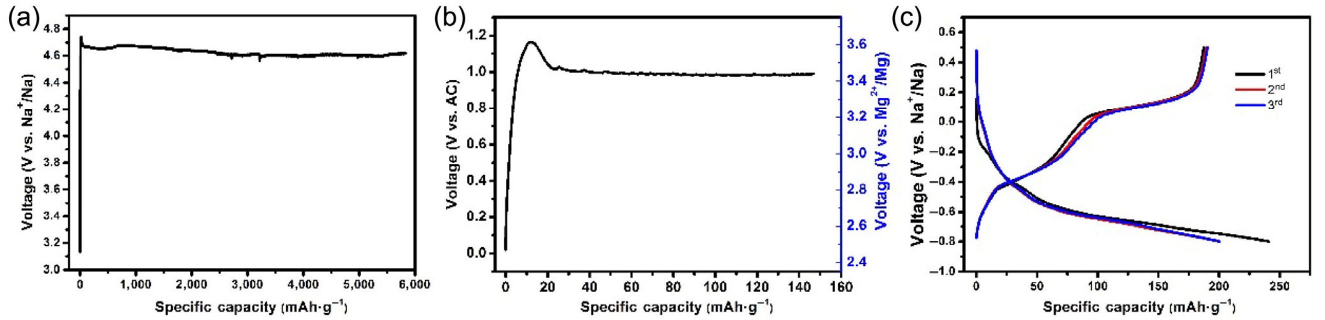

Figure 7 (a) The charge curve of NVO in Na ion battery. (b) The charge curve of NVO in Mg battery. (c) The discharge and charge curves of NVO after cycling in Mg battery.

indicating the Na$^+$ in NVO is electrochemically stable. Moreover, we also study the stability of Na$^+$ in NVO in RMBs. Similarly, the extraction of Na$^+$ is not observed during the directly charging process (Fig. 7(b)). In addition, in order to prove there is no extraction of Na$^+$ after insertion of Mg^{2+}, the NVO electrode cycled after 5 cycles has been washed, dried then reassembled into a new magnesium battery to perform the insertion and extraction of Mg^{2+}, as shown in Fig. 7(c). The discharge and charge curves are not changed, and the cycled NVO can work normally as before, indicating there is no extraction of Na$^+$. Furthermore, we also confirm the presence of Na in the NVO electrode after 50 cycles. As described in Fig. S5 in the ESM, all of the Na, V and O elements are observed, indicating Na$^+$ is present in NVO during the discharge and charge processes. Moreover, as shown in Table S3 in the ESM, the results of ICP also confirm the stability of Na in NVO.

4 Conclusion

In summary, the NVO has been synthesized successfully and studied as the cathode of RMBs. The NVO exhibits a high specific capacity of 213.4 mAh·g^{-1} at 10 mA·g^{-1} with a high working voltage (above 1.6 V vs. Mg^{2+}/Mg), and shows remarkable long-term cyclic stability of 119.2 mAh·g^{-1} after 100 cycles at 20 mA·g^{-1}. It is worth noted that the NVO presents an impressive rate capacity, and the discharge capacities of NVO are 210.1, 137.0, 111.7, 80.2, 52.3, and 27.2 mAh·g^{-1} at 10, 20, 50, 100, 200, and 500 mA·g^{-1}, respectively. When the current density return to 20 mA·g^{-1}, the NVO electrode delivers a high specific capacity of around 140 mAh·g^{-1}, indicating the high reversibility and high diffusion of Mg^{2+}. These have been confirmed by subsequent GITT and EIS tests. The intercalation/extraction mechanism has been proved by *ex-situ* characterizations. Furthermore, the DFT calculation results show that Mg^{2+} tends to occupy the semi-occupied sites of Na in the NVO. After cycling, the NVO still presents an excellent crystal stability. Moreover, the main role of Na in NVO, as mentioned in the text, is as follows: (i) the introduction of Na between the V_2O_5 layers can increase the interlayer spacing and increase the diffusion kinetics of Mg^{2+}. (ii) Na$^+$ between layers as a support, which improves the stability of the NVO layered structure. Besides, we have also confirmed the stability of Na$^+$ in NVO during the electrochemical behavior. In conclusion, the application of NVO in RMBs successfully increases the energy density of the system, making the RMBs strive to develop toward high energy density. At the same time, we have also proved that this kind of material has a non-negligible position in the cathode materials of RMBs, which provides valuable experience for later research and development of more cathode materials for RMBs.

Acknowledgements

We gratefully acknowledge the financial support from the National Natural Science Foundation of China (Nos. 21875198 and 21621091). The authors also would like to thank Prof. D. W. Liao for his valuable suggestions and guidance.

Electronic Supplementary Material: Supplementary material (EDS mapping, the electrochemical performance of Mg full cell, XRD pattern, comparison of some previous work, EIS fitted data) is available in the online version of this article at https://doi.org/10.1007/s12274-019-2602-6.

References

[1] Etacheri, V.; Marom, R.; Elazari, R.; Salitra, G.; Aurbach, D. Challenges in the development of advanced Li-ion batteries: A review. *Energy Environ. Sci.* **2011**, *4*, 3243–3262.

[2] Goodenough, J. B.; Park, K. S. The Li-ion rechargeable battery: A perspective. *J. Am. Chem. Soc.* **2013**, *135*, 1167–1176.

[3] Liu, N.; Lu, Z. D.; Zhao, J.; McDowell, M. T.; Lee, H. W.; Zhao, W. T.; Cui, Y. A pomegranate-inspired nanoscale design for large-volume-change lithium battery anodes. *Nat. Nanotechnol.* **2014**, *9*, 187–192.

[4] McCalla, E.; Abakumov, A. M.; Saubanère, M.; Foix, D.; Berg, E. J.; Rousse, G.; Doublet, M. L.; Gonbeau, D.; Novák, P.; van Tendeloo, G. et al. Visualization of O-O peroxo-like dimers in high-capacity layered oxides for Li-ion batteries. *Science* **2015**, 350, 1516–1521.

[5] Wen, Z.; Yeh, M. H.; Guo, H. Y.; Wang, J.; Zi, Y. L.; Xu, W. D.; Deng, J. A.; Zhu, L.; Wang, X.; Hu, C. G. et al. Self-powered textile for wearable electronics by hybridizing fiber-shaped nanogenerators, solar cells, and supercapacitors. *Sci. Adv.* **2016**, *2*, e1600097.

[6] Zhao, J. H.; Kang, T.; Chu, Y. L.; Chen, P.; Jin, F.; Shen, Y. B.; Chen, L. W. A polyimide cathode with superior stability and rate capability for lithium-ion batteries. *Nano Res.* **2019**, *12*, 1355–1360.

[7] Chen, S. L.; Zou, J.; Li, Y. H.; Li, N.; Wu, M.; Lin, J. H.; Zhang, J. M.; Cao, J.; Feng, J. C.; Niu, X. B. et al. Atomic-scale structural and chemical evolution of $Li_3V_2(PO_4)_3$ cathode cycled at high voltage window. *Nano Res.* **2019**, *12*, 1675–1681.

[8] Muldoon, J.; Bucur, C. B.; Gregory, T. Quest for nonaqueous multivalent secondary batteries: Magnesium and beyond. *Chem. Rev.* **2014**, *114*, 11683–11720.

[9] Wang, Y.; Wang, C.; Yi, X.; Hu, Y.; Wang, L.; Ma, L.; Zhu, G.; Chen, T.; Jin, Z. Hybrid Mg/Li-ion batteries enabled by Mg^{2+}/Li$^+$ co-intercalation in VS_4 nanodendrites. *Energy Storage Materials* **2019**, *23*, 741–748.

[10] Wang, Y.; Liu, Z.; Wang, C.; Yi, X.; Chen, R.; Ma, L.; Hu, Y.; Zhu, G.; Chen, T.; Tie, Z.; et al. Highly branched VS_4 nanodendrites with 1D atomic-chain structure as a promising cathode material for long-cycling magnesium batteries. *Adv. Mater.* **2018**, *30*, 1802563.

[11] Wang, Y.; Chen, R.; Chen, T.; Lv, H.; Zhu, G.; Ma, L.; Wang, C.; Jin, Z.; Liu, J. Emerging non-lithium ion batteries. *Energy Storage Materials* **2016**, *4*, 103–129.

[12] Wang, Y.; Xue, X.; Liu, P.; Wang, C.; Yi, X.; Hu, Y.; Ma, L.; Zhu, G.; Chen, R.; Chen, T.; et al. Atomic substitution enabled synthesis of vacancy-rich two-dimensional black TiO_{2-x} nanoflakes for high-performance rechargeable magnesium batteries. *ACS Nano* **2018**, *12*, 12492–12502.

[13] Shterenberg, I.; Salama, M.; Gofer, Y.; Levi, E.; Aurbach, D. The challenge of developing rechargeable magnesium batteries. *MRS Bull.* **2014**, *39*, 453–460.

[14] Koketsu, T.; Ma, J. W.; Morgan, B. J.; Body, M.; Legein, C.; Dachraoui, W.; Giannini, M.; Demortière, A.; Salanne, M.; Dardoize, F. et al. Reversible magnesium and aluminium ions insertion in cation-deficient anatase TiO_2. *Nat. Mater.* **2017**, *16*, 1142–1148.

[15] Zhang, R. G.; Arthur, T. S.; Ling, C.; Mizuno, F. Manganese dioxides as rechargeable magnesium battery cathode; synthetic approach to understand magnesiation process. *J. Power Sources* **2015**, *282*, 630–638.

[16] Amatucci, G. G.; Badway, F.; Singhal, A.; Beaudoin, B.; Skandan, G.; Bowmer, T.; Plitz, I.; Pereira, N.; Chapman, T.; Jaworski, R. Investigation of yttrium and polyvalent ion intercalation into nanocrystalline vanadium oxide. *J. Electrochem. Soc.* **2001**, *148*, A940–A950.

[17] Xue, X. L.; Chen, R. P.; Yan, C. Z.; Zhao, P. Y.; Hu, Y.; Kong, W. H.; Lin, H. N.; Wang, L.; Jin, Z. One-step synthesis of 2-ethylhexylamine pillared vanadium disulfide nanoflowers with ultralarge interlayer spacing for high-performance magnesium storage. *Adv. Energy Mater.* **2019**, *9*, 1900145.

[18] NuLi, Y.; Zheng, Y. P.; Wang, Y.; Yang, J.; Wang, J. L. Electrochemical intercalation of Mg^{2+} in 3D hierarchically porous magnesium cobalt silicate and its application as an advanced cathode material in rechargeable magnesium batteries. *J. Mater. Chem.* **2011**, *21*, 12437–12443.

[19] Ma, Z.; MacFarlane, D. R.; Kar, M. Mg cathode materials and electrolytes for rechargeable Mg batteries: A review. *Batter. Supercaps.* **2019**, *2*, 115–127.

[20] Zhang, R. G.; Ling, C. Unveil the chemistry of olivine $FePO_4$ as magnesium battery cathode. *ACS Appl. Mater. Interfaces* ***2016**, 8, 1801*8**–180**26.

[21] Aurbach, D.; Lu, Z.; Schechter, A.; Gofer, Y.; Gizbar, H.; Turgeman, R.; Cohen, Y.; Moshkovich, M.; Levi, E. Prototype systems for rechargeable magnesium batteries. *Nature* **2000**, *407*, 724–727.

[22] Xiong, F. Y.; Fan, Y. Q.; Tan, S. S.; Zhou, L. M.; Xu, Y. Y.; Pei, C. Y.; An, Q. Y.; Mai, L. Q. Magnesium storage performance and mechanism of CuS cathode. *Nano Energy* **2018**, *47*, 210–216.

[23] Zhang, R. G.; Yu, X. Q.; Nam, K. W.; Ling, C.; Arthur, T. S.; Song, W.; Knapp, A. M.; Ehrlich, S. N.; Yang, X. Q.; Matsui, M. α-MnO_2 as a cathode material for rechargeable Mg batteries. *Electrochem. Commun.* **2012**, *23*, 110–113.

[24] Cao, A. M.; Hu, J. S.; Liang, H. P.; Wan, L. J. Self-assembled vanadium pentoxide (V_2O_5) hollow microspheres from nanorods and their application in lithium-ion batteries. *Angew. Chem., Int. Ed.* **2005**, *44*, 4391–4395.

[25] Liu, J.; Xia, H.; Xue, D. F.; Lu, L. Double-shelled nanocapsules of V_2O_5-based composites as high-performance anode and cathode materials for Li ion batteries. *J. Am. Chem. Soc.* **2009**, *131*, 12086–12087.

[26] Su, D. W.; Wang, G. X. Single-crystalline bilayered V_2O_5 nanobelts for high-capacity sodium-ion batteries. *ACS Nano* **2013**, *7*, 11218–11226.

[27] Novák, P.; Desilvestro, J. Electrochemical insertion of magnesium in metal oxides and sulfides from aprotic electrolytes. *J. Electrochem. Soc.* **1993**, *140*, 140–144.

[28] Novák, P.; Scheifele, W.; Joho, F.; Haas, O. Electrochemical insertion of magnesium into hydrated vanadium bronzes. *J. Electrochem. Soc.* **1995**, *142*, 2544–2550.

[29] Gautam, G. S.; Canepa, P.; Malik, R.; Liu, M.; Persson, K.; Ceder, G. First-principles evaluation of multi-valent cation insertion into orthorhombic V_2O_5. *Chem. Commun.* **2015**, *51*, 13619–13622.

[30] Sai Gautam, G.; Canepa, P.; Richards, W. D.; Malik, R.; Ceder, G. Role of structural H_2O in intercalation electrodes: The case of Mg in nanocrystalline xerogel-V_2O_5. *Nano Lett.* **2016**, *16*, 2426–2431.

[31] Yu, L.; Zhang, X. G. Electrochemical insertion of magnesium ions into V_2O_5 from aprotic electrolytes with varied water content. *J. Colloid Interface Sci.* **2004**, *278*, 160–165.

[32] Perera, S. D.; Archer, R. B.; Damin, C. A.; Mendoza-Cruz, R.; Rhodes, C. P. Controlling interlayer interactions in vanadium pentoxide-poly(ethylene oxide) nanocomposites for enhanced magnesium-ion charge transport and storage. *J. Power Sources* **2017**, *343*, 580–591.

[33] Rashad, M.; Zhang, H. Z.; Asif, M.; Feng, K.; Li, X. F.; Zhang, H. M. Low-cost room-temperature synthesis of $NaV_3O_8\cdot1.69H_2O$ nanobelts for Mg batteries. *ACS Appl. Mater. Interfaces* **2018**, *10*, 4757–4766.

[34] Tang, H.; Xiong, F. Y.; Jiang, Y. L.; Pei, C. Y.; Tan, S. S.; Yang, W.; Li, M. S.; An, Q. Y.; Mai, L. Q. Alkali ions pre-intercalated layered vanadium oxide nanowires for stable magnesium ions storage. *Nano Energy* **2019**, *58*, 347–354.

[35] Deng, X. W.; Xu, Y. A.; An, Q. Y.; Xiong, F. Y.; Tan, S. S.; Wu, L. M.; Mai, L. Q. Manganese ion pre-intercalated hydrated vanadium oxide as a high-performance cathode for magnesium ion batteries. *J. Mater. Chem. A* **2019**, *7*, 10644–10650.

[36] Cabello, M.; Nacimiento, F.; Alcántara, R.; Lavela, P.; Ortiz, G.; Tirado, J. L. Nanobelts of beta-sodium vanadate as electrode for magnesium and dual magnesium-sodium batteries. *J. Electrochem. Soc.* **2016**, *163*, A2781–A2790.

[37] Gershinsky, G.; Yoo, H. D.; Gofer, Y.; Aurbach, D. Electrochemical and spectroscopic analysis of Mg^{2+} intercalation into thin film electrodes of layered oxides: V_2O_5 and MoO_3. *Langmuir* **2013**, *29*, 10964–10972.

[38] Jiang, D. L.; Wang, H.; Li, G. P.; Li, G. Q.; Lan, X. Z.; Abib, M. H.; Zhang, Z. P.; Jiang, Y. Self-combustion synthesis and ion diffusion performance of NaV_6O_{15} nanoplates as cathode materials for sodium-ion batteries. *J. Electrochem. Soc.* **2015**, *162*, A697–A703.

[39] Kresse, G.; Furthmüller, J. Efficient iterative schemes for *ab initio* total-energy calculations using a plane-wave basis set. *Phys. Rev. B* **1996**, *54*, 11169–11186.

[40] Perdew, J. P.; Burke, K.; Ernzerhof, M. Generalized gradient approximation made simple. *Phys. Rev. Lett.* **1996**, *77*, 3865–3868.

[41] Blöchl, P. E. Projector augmented-wave method. *Phys. Rev. B* **1994**, *50*, 17953–17979.

[42] Dudarev, S. L.; Botton, G. A.; Savrasov, S. Y.; Humphreys, C. J.; Sutton, A. P. Electron-energy-loss spectra and the structural stability of nickel oxide: An LSDA+U study. *Phys. Rev. B* **1998**, *57*, 1505–1509.

[43] Monkhorst, H. J.; Pack, J. D. Special points for Brillouin-zone integrations. *Phys. Rev. B* **1976**, *13*, 5188–5192.

[44] Momma, K.; Izumi, F. *VESTA*: A three-dimensional visualization system for electronic and structural analysis. *J. Appl. Cryst.* **2008**, *41*, 653–658.

[45] Pereira-Ramos, J. P.; Messina, R.; Znaidi, L.; Baffier, N. Electrochemical lithium intercalation in $Na_{0.33}V_2O_5$ bronze prepared by sol-gel processes. *Solid State Ionics* **1988**, *28*, 886–894.

[46] Wang, Y. R.; Xue, X. L.; Liu, P. Y.; Wang, C. X.; Yi, X.; Hu, Y.; Ma, L. B.; Zhu, G. Y.; Chen, R. P.; Chen, T. et al. Atomic substitution enabled synthesis of vacancy-rich two-dimensional black TiO_{2-x} nanoflakes for high-performance rechargeable magnesium batteries. *ACS Nano* **2018**, *12*, 12492–12502.

[47] Cabello, M.; Alcántara, R.; Nacimiento, F.; Lavela, P.; Aragón, M. J.; Tirado, J. L. $Na_3V_2(PO_4)_3$ as electrode material for rechargeable magnesium batteries: A case of sodium-magnesium hybrid battery. *Electrochim. Acta* **2017**, *246*, 908–913.

[48] Tang, H.; Peng, Z.; Wu, L.; Xiong, F. Y.; Pei, C. Y.; An, Q. Y.; Mai, L. Q. Vanadium-based cathode materials for rechargeable multivalent batteries: Challenges and opportunities. *Electrochem. Energy Rev.* **2018**, *1*, 169–199.

[49] Liu, H. M.; Wang, Y. G.; Li, L.; Wang, K. X.; Hosono, E.; Zhou, H. S. Facile synthesis of NaV_6O_{15} nanorods and its electrochemical behavior as cathode material in rechargeable lithium batteries. *J. Mater. Chem.* **2009**, *19*, 7885–7891.

[50] Liu, H. M.; Zhou, H. S.; Chen, L. P.; Tang, Z. F.; Yang, W. S. Electrochemical insertion/deinsertion of sodium on NaV_6O_{15} nanorods as cathode material of rechargeable sodium-based batteries. *J. Power Sources* **2011**, *196*, 814–819.

[51] Zhao, M. S.; Zhang, W. G.; Song, X. P. Lithium-ion storage properties of a micro/nanosheet-like NaV_6O_{15} anode in aqueous solution. *Dalton Trans*. **2017**, *46*, 3857–3863.

[52] Prosini, P. P.; Lisi, M.; Zane, D.; Pasquali, M. Determination of the chemical diffusion coefficient of lithium in $LiFePO_4$. *Solid State Ionics* **2002**, *148*, 45–51.

[53] Rui, X. H.; Ding, N.; Liu, J.; Li, C.; Chen, C. H. Analysis of the chemical diffusion coefficient of lithium ions in $Li_3V_2(PO_4)_3$ cathode material. *Electrochim. Acta* **2010**, *55*, 2384–2390.

[54] Zeng, J.; Wu, D. Z.; Wang, X.; Wu, J. N.; Li, J. Y.; Wang, J.; Zhao, J. B. Insights into the Mg storage property and mechanism based on the honeycomb-like structured $Na_3V_2(PO_4)_3$/C/G in anhydrous electrolyte. *Chem*. *Eng*. *J*. **2019**, *372*, 37–45.

[55] Zeng, J.; Yang, Y.; Lai, S. B.; Huang, J. X.; Zhang, Y. Y.; Wang, J.; Zhao, J. B. A promising high-voltage cathode material based on mesoporous $Na_3V_2(PO_4)_3$/C for rechargeable magnesium batteries. *Chem*. *–Eur*. *J*. **2017**, *23*, 16898–16905.

[56] Yang, Y.; Huang, J. X.; Zeng, J.; Xiong, J.; Zhao, J. B. Direct electrophoretic deposition of binder-free Co_3O_4/graphene sandwich-like hybrid electrode as remarkable lithium ion battery anode. *ACS Appl*. *Mater*. *Interfaces* **2017**, *9*, 32801–32811.